ORIGINAL RESEARCH ARTICLE

Micromechanical Characterization of 10 MeV High-Energy Fe^+ Ion-Irradiated NiTi SMA in Two-Direction Nanoindentation Tests

N. LEVINTANT-ZAYONTS, I. JOZWIK, W. CHROMINSKI, S.S. AKHMADALIEV, and S. KUCHARSKI

The objective of the present study is to investigate the hardening behavior, superelastic recovery, and structural properties of NiTi Shape Memory Alloy (SMA) after 10 MeV high-energy Fe^+ ion irradiation to damage levels of 1.2 and 6.0 d.p.a (displacements per atom). According to Stopping and Range of Ions in Matter (SRIM) calculations, Secondary Ion Mass Spectroscopy (SIMS) analysis, and Transmission Electron Microscopy (TEM) imaging, a 3-micron irradiation layer was obtained with an amorphous structure; the maximum values of damage and Fe^+ ion concentration occurred at 2.4 and 2.7 microns, respectively. The mechanical response was characterized in two-direction nanoindentation tests: parallel and perpendicular to the ion beam direction. Cross-sectional nanoindentation indicates that the maximum hardening corresponds to the maximum of the Fe^+ ion concentration; the maximum hardness was found at 2.7 microns for both d.p.a. levels. The changes in superelastic properties were achieved in the amorphous layer that suppressed the B2-B19′ phase transformation at a sub-micron scale. We show that cross-sectional nanoindentation is an appropriate method for determining the subtle micromechanical property changes in near-surface regions. It also allows the material and structural properties at a selected point in the non-homogeneous irradiated layer to be correlated with the local level of irradiation damage or ion concentration. This is very important in the development of SMAs and their applications in nuclear technologies.

https://doi.org/10.1007/s11661-025-07931-0

I. INTRODUCTION

SHAPE Memory Alloys (SMAs) have unique properties, such as superelasticity (SE) and the shape memory effect (SME), which are caused by the reversible martensitic transformation between the austenite B2 cubic structure phase and the martensite B19′ monoclinic structure phase, mainly by shearing. SMAs can carry large strains when a force is applied and recover their prior shape and dimensions upon release of the force or the application of heat.[1–4] Due to their unique properties, SMAs have many applications in medical devices, actuators, and robotic industries. They now have potential applications for aerospace technology and fusion engineering in the nuclear industry.[5–7] In nuclear applications, NiTi-based SMAs show great potential for actuation, sensing, and damping applications. During their usage in nuclear applications, SMAs may be subjected to irradiation, which may affect their structure and, eventually, their functional properties.[8–14]

Irradiation-induced damage leads to changes in the mechanical properties of irradiated materials and is one of the major safety issues in the nuclear industry.[15–17] Understanding irradiation-induced material degradation is important, not only to the development of new materials for nuclear applications but, also, to the extension of the operating lifetimes of currently operational nuclear reactors. Since there are difficulties in exploring the effects of neutron irradiation (*e.g.*, the long time periods needed to achieve high doses and the

N. LEVINTANT-ZAYONTS is with the Institute of Fundamental Technological Research, PAS, A. Pawinskiego 5B, 02-108 Warsaw, Poland and also with the Institute of Fundamental Technological Research, Pawinskiego 5B, 02-106 Warsaw, Poland. Contact e-mail: neonila@ippt.pan.pl I. JOZWIK is with the NOMATEN Centre of Excellence, National Centre for Nuclear Research, A. Soltana 7, 05-400 Otwock, Poland. W. CHROMINSKI is with the NOMATEN Centre of Excellence, National Centre for Nuclear Research and also with the Warsaw University of Technology Faculty of Materials Science and Engineering, Wołoska 141, 02-507 Warsaw, Poland. S.S. AKHMADALIEV is with the Ion Beam Centre of Helmholtz Zentrum Dresden-Rossendorf, Bautzner Landstraße 400, 01328 Dresden, Germany. S. KUCHARSKI is with the Institute of Fundamental Technological Research, PAS.
Manuscript submitted February 27, 2025; accepted July 27, 2025.

Published online: 05 August 2025

handling of harmful radioactive material), ion irradiation (ion implantation) is a widely used means of inducing irradiation damage in materials, as a substitute for neutron irradiation.[17] Ion irradiation can produce high damage levels without residual radioactivity over a short period of time; however, ion-irradiated layers have limited thickness, from several hundred nanometers to a few micrometers.[18,19] In this regard, the combination of small and ultra-small-scale mechanical testing has become a powerful tool for the evaluation of irradiation-induced mechanical property changes. Reviews have already been published, with respect to experimental methods such as nanoindentation, micro-pillar compression, micro-tension, and micro-cantilever bending but these were mainly concerned with classical materials for general engineering (and nuclear engineering, to a lesser extent).[20–27]

For SMA, the nanoindentation results are difficult to interpret because, in these materials, different mechanisms of deformation may occur, other than those observed in classical elasto-plastic materials.[28] Even a determination of fundamental material parameters, such as hardness or elastic modulus, is not obvious. For example, it was concluded that the use of the conventional Oliver–Pharr (O-P) method for SMA may generate errors of up to 16 and 40 pct in hardness and modulus, respectively. Therefore, Gao *et al.*[28,29] provided correction factors for the O-P method in the numerical simulation of Berkovich indentation tests in SMA.

Recent studies on ion-irradiated NiTi SMA have focused on the effects of high-energy irradiation on the structure, mechanical properties, and phase-transformation characteristics. A 3-μm-thick modified layer was observed in martensitic NiTi, consisting of TiH_2, bcc, and fcc phases after irradiation with 3 MeV protons.[30] Afzal *et al.* demonstrated that the 2 MeV proton irradiation of austenitic NiTi produced lattice disorder (using the tension test at room temperature with a speed of 0.5 mm/min) and a new rhombohedral R phase was formed. An increase in Vickers hardness has also been observed.[31] Wang at al. investigated the microstructure of martensitic NiTi after 3 MeV proton irradiation up to a fluence of 10^{16} cm^{-2}. In a region approximately 3 μm from the surface, a multilayer structure (including B2 phase, Ti2Ni ,and TiH2 phases) was created and the ratio of Ti to Ni was no longer equiatomic. The stress–strain curves for irradiated samples showed an increase in phase-transformation stress and tensile fracture strength.[32] A study of a martensitic microstructure modified by Ni^+ ion irradiation to 1×10^{14} and 5×10^{15} cm^{-2} with an energy of 5 MeV showed that NiTi readily amorphizes at relatively low fluences of high-energy particles.[33] TEM images showed an amorphous layer with a thickness of 1.75 μm. Monoclinic and BCC nanocrystals were observed in this layer, as well as a sharp interface between amorphous (irradiated layer) and crystalline material (undamaged). According to the authors, the most likely mechanism for amorphization is the combination of cascade overlapping and damage accumulation.[33] TEM cross-sectional observations indicated that after 5 MeV and 10^{14} cm^{-2} Ni^+ ion irradiation, a maximum amorphous fraction in martensitic NiTi was observed at the depth of 1.2 μm, which was 0.7 μm shallower than the depth of the maximum Ni^+ concentration. Thin 8 μm NiTi films were irradiated with 80 MeV Ar^+ and 40 MeV Ne^+ ions to fluencies of 1×10^{15} cm^{-2}. X-ray diffraction showed that both irradiations induced a martensite (B19′) to austenite (B2) transformation in the samples and considerable amorphization (37 vol. pct) was observed in the case of the Ar^+ ion irradiation. No noticeable amorphization was detected for 40 MeV Ne^+-irradiated samples.[34] Amorphous fractions in Au^+ ion-irradiated NiTi (martensite) at 350 MeV were also observed.[35] *In situ* TEM investigations showed that Xe^+ samples irradiated at an energy of 400 keV TiNiCu were already amorphized at 0.4 d.p.a. at a depth of 68 nm. The authors concluded that the amorphous transition was due to chemical disordering, resulting from displacement cascades.[36] Amorphous phases in the NiTi induced by 2 MeV proton irradiation were noticed in the TEM observations made by Cheng and Ardell.[37] The irradiated region contains two layers: the first being nearer to the free surface and consisting of a mixture of amorphous and crystalline phases. The second layer, beneath the first, was completely transformed to the amorphous phase. The critical dose required for complete amorphization was estimated to be 0.25 d.p.a.[37] and so even a low d.p.a. destroys the SMA structure and may significantly affect the martensitic transformation of these materials. Grummon and Gotthardt applied doses of 0.1 to 0.5 d.p.a. of Ni^+ ion irradiation at 5 MeV, to modify the martensitic phase transformation in thin 6 μm NiTi samples and to develop the actuator conception of NiTi SMA in a cyclic bending test.[38] A 1.5-μm-thick beam damage zone was obtained. Using Berkovich nanoindentation tests, they showed that 5 MeV Ni^+ ion irradiation results in an, approximately, twofold increase in Young's modulus and a threefold increase in hardness. Hinojos *et al.* applied a high energy of 30 MeV Ni^+ (10^{13} cm^{-2} corresponding to 0.08 d.p.a.) to evaluate the influence of radiation defects on mechanical properties and on the martensitic transformation in NiTi.[39] High-resolution STEM imaging revealed that the damage was distributed inhomogeneously, comprising a mixture of amorphous clusters and crystalline B2 phase in the implanted region. According to the SRIM code, the peak damage of 0.08 d.p.a. was located at a depth of ~ 4.9 μm, which was below the reported critical amorphization threshold. The Berkovich nanoindentation showed that, to achieve the B2-B19′ martensitic transformation in ion-irradiated NiTi, an increase in load was needed. It also showed that the irradiated NiTi was 50 pct harder and retained less recoverable displacement (around 85 pct) than non-implanted samples. The results suggest the potential for Ni^+ ion beam modification to achieve the functional surface modification of NiTi.[39]

As described above, nanoindentation is a promising method for studying the mechanical properties of ion-irradiated materials, in the context of nuclear applications. For nanoindentation tested SMAs, the

relations between structure, superelasticity phenomena, and hardness are complex; they are further complicated by the influence of ion irradiation. The interrelation between implanted layer thickness, its structure, and hardness distribution over indentation depth are unclear. The main aim of studying irradiated materials is to evaluate hardness over a wide range of doses. There is still a lack of understanding as to how high-energy ion irradiation impacts the functional properties of SMA at different levels of d.p.a.

According to the review presented above, when the implanted ions and d.p.a. distributions are highly inhomogeneous, then the hardness determined from the indentation along the direction of the ion beam corresponds to the averaged properties and cannot be attributed to the actual values of the ion concentration and d.p.a. level. Therefore, the aim of our study is to investigate SMA's mechanical response in two-direction nanoindentation tests, comprising conventional tests along the ion beam direction (as a function of indentation depth) and cross-sectional nanoindentation, perpendicular to the ion beam direction (as a function of distance from the surface). A comparison between commonly used nanoindentation (where indents are made along the ion beam) with cross-sectional analysis (when the indents are made perpendicular to the ion beam direction) is presented. We discuss the benefits and disadvantages of both indentation methods and demonstrate the advantages of a cross-sectional indentation approach. The local superelastic behavior of NiTi SMA, after 10 MeV high-energy Fe^+ ion implantation, is presented, as well as its mechanical (nanomechanical) and structural (nanostructural) properties.

II. MATERIALS AND EXPERIMENTAL PROCEDURES

In this study, a commercial Ni − 50.7 at. pct Ti (NiTi, NITINOL) shape memory alloy was used. The samples were flat and cut into 10 × 10 × 0.7 mm coupons. The sample surfaces were mechanically polished using a polish diamond compound (3 and 1 μm) and finished with an Al_2O_3 suspension. Differential Scanning Calorimetry (DSC, Pyris-1) was used to specify the characteristic (phase transformation) temperatures. The measurements were carried out at heating and cooling rates of 10 °C/min, within the temperature range − 60 °C to 100 °C.

NiTi samples were irradiated with Fe^+ ions up to fluences of 1×10^{15} and 5×10^{15} cm^{-2}. During irradiation, half of each sample was covered with a conductive material to ensure the same thermal history for the irradiated and pristine material during irradiation. The irradiation experiments were conducted using 10 MeV Fe^+ ion beams, at the Helmholtz-Zentrum Dresden-Rossendorf (HZDR) of the Central Institute for Nuclear Research.

The mean projected range of Fe ions and damage distribution in NiTi were estimated using an SRIM code.[40] A full collision cascade mode was used and the displacement energies were set as SRIM default values (20 eV) for both Ni and Ti atoms.

In order to experimentally determine the penetration depth of Fe ions, Secondary Ion Mass Spectroscopy (SIMS, CAMECA IMS 6F) measurements were carried out. A Cs beam with a current of 50 nA and energy of 5.5 keV was used for the analysis. An area of 200 × 200 μm was scanned and the data from the central 60 μm diameter were analyzed.

Mechanical properties of the implanted layer were determined using a commercial, extremely low load indentation system: the Ultra-Nano-Indenter (UNHT, CSM, Instruments SA) with a Berkovich tip.

The hardness measurements were carried out by two-direction nanoindentation tests and, in both cases, the hardness was calculated using the Oliver–Pharr method.[41] In the first direction (parallel to the ion beam), conventional test nanohardness measurements were undertaken as a function of indentation depth. The loads of 0.2, 1.0, 1.5, 2.5, 3.5, and 5.0 mN were applied for indentation on the non-implanted and ion-implanted surfaces. The tests were repeated five to seven times for each force, in order to limit the influence of material inhomogeneities. In the second direction (perpendicular to the ion beam), nanohardness measurements were undertaken as a function of distance from the surface in the cross-sectional nanoindentation, carried out by employing a single, low load of 0.2 mN. The test was performed on the cross-section surface, along the measurement line (indent row), but deviated 12 deg from the implanted surface line. Such indenting enabled direct access to the particular regions of the irradiated layer. A probing step was taken at 0.27 μm, in order to repeatedly probe; seven indent rows were made.

The NiTi samples were prepared for cross-sectional indentation using a broad ion beam polishing system (Hitachi IM4000, Ar^+) and then the samples were securely mounted in steel clamps to prevent deformation and ensure reliable measurements near the specimen edges.

Scanning electron microscopy (SEM) imaging was conducted using a Helios 5 UX Dual Beam system (ThermoFisher Scientific) equipped with SE, BSE, and STEM detectors. The same system was employed for electron-transparent lamella preparation, using the focused ion beam (FIB) lift-out technique. Structural analysis of the irradiated samples was carried out using a JEOL JEM-F200 transmission electron microscope (TEM).

III. RESULTS AND DISCUSSION

A. *Characterization of Initial and Fe^+ Ion-Irradiated NiTi SMA*

1. *Sequence of phase transformation and NiTi structure*

In the case of alloys exhibiting the shape memory effect (SME), the temperature values (*Ms*, *Mf*, *As*, and *Af*) at which phase transformations occur are extremely

important. The definitions of these temperatures are as follows:

- *Ms*—start of the martensitic phase formation in the cooling process (B2 → B19′);
- *Mf*—end of the martensitic phase formation in the cooling process (B2 → B19′);
- *As*—start of the austenitic phase formation in the heating process (B19′ → B2);
- *Af*—end of the austenitic phase formation in the heating process (B19′ → B2).

The temperature range and scan rates in the DSC test are presented lower.

Figure 1 shows the evolution of the DSC cooling/heating curve for virgin NiTi. It can be seen that the NiTi alloy transforms in one step during both cooling and heating; the characteristic temperatures were $Ms = 15.9$ °C; $Mf = -1.6$ °C; $As = 3.6$ °C; $Af = 19$ °C. Because the austenite finishing temperature ($Af = 19$ °C) was lower than room temperature ($T_R = 24$ °C), the examined NiTi was in the austenitic phase and exhibited superelastic behavior. This was also confirmed by the results from TEM diffraction, showing the presence of NiTi B2 phase [Figure 1(c)]. The irradiation temperature was maintained at about 90 °C, which was well above *Af*. Thus, the NiTi samples were kept in the austenitic phase state during the irradiation.

Considering the effect of ion irradiation on the characteristic temperatures, it should be pointed out that the problem is more complex and there are some nuances that cannot be ignored. Our previous research reported that the characteristic temperatures of NiTi were distinctly shifted to higher temperatures as a result of the nitrogen ion irradiation of NiTi at 55-60 keV. The participation of the implanted layer in the measured volume was then 0.09 pct, so we attributed the change of the characteristic temperatures to the increased temperature during implantation.[42,43] Certainly, in the present study, the internal stress and modified composition of the irradiated layer (approximately 3 μm) disrupt the NiTi structure and modify its thermodynamic properties. This can affect the phase-transformation ability in the near-surface zone. However, the contribution of the irradiated layer (~ 3 μm) of the investigated sample with thin of 700 μm to the thermodynamic response in the DSC test was ~ 0.38 pct. Each change in the size of the substrate will cause changes in the DSC results. The effect of complex phenomena on the thin near-surface region of NiTi SMA (after ion irradiation) and the characteristic temperatures is a separate issue, which requires additional, more specific research.

2. *Depth Profile Analysis*

According to the SRIM simulations, a projected range of the Fe ions equals about 2.47 μm, with a maximum concentration of Fe atoms of 0.24 and 1.2 pct, for 1×10^{15} and 5×10^{15} cm^{-2}, respectively. The highest level of radiation damage is located slightly shallower than the maximum of the Fe ion distribution and corresponds to 1.2 and 6.0 d.p.a. for the two cases, see Figure 2.

The SIMS analysis was used to determine the variation of the elemental components in the NiTi samples with depth, before and after Fe^+ ion irradiation. Depth distributions of the chemical composition are shown in Figures 3(a) through (c), for non-implanted NiTi and Fe implanted to 1.2 and 6.0 d.p.a., respectively.

The maximum penetration depth of the iron ions is approximately 2.5 and 2.7 μm for doses of 1.2 and 6.0 d.p.a., respectively, as shown in Figures 3(b) and (c). A redistribution of Ni and Ti elements can be observed. The lower SIMS signals for these elements were detected through the investigated thickness for both doses but for Ti, the reduction is more distinct. A very slight decrease in Ni and Ti contents occurs at depths corresponding to the maximum iron concentration for a dose of 1.2 d.p.a. However, for samples implanted up to 6.0 d.p.a., the changes in Ni and Ti concentrations are detected at depths of about 3.2 μm. In both cases, the decrease of Ni and Ti concentrations at the maximum Fe concentration are barely visible.

Oxygen contamination is observed across the investigated thickness of all samples. A higher value of the SIMS signal for oxygen was detected at the non-implanted surface, as marked on the right axis in Figure 3(a). A decrease in the SIMS signal with depth, in the oxygen profile, is visible for both implanted layers.

3. *TEM observations of Fe ion-irradiated NiTi*

Thin specimens were prepared for TEM analysis using the FIB lift-out technique, by selectively milling electron-transparent 'windows' along the whole of the irradiated depth. In both studied cases of irradiation levels (1.2 and 6.0 d.p.a.), the TEM analysis revealed the full amorphization of the irradiated layer (Figure 4). Figure 4 shows the boundary between the amorphous layer and crystalline regions. The boundary lies approximately 3.5 μm below the surface of the sample. The red rings in Figure 4 indicate the locations of the diffraction aperture used to capture the diffraction patterns. It is clear that the lower region, with a homogenous contrast, is amorphous, since electron diffraction forms continuous diffusive rings. Directly beneath the amorphous region, the B2 cubic phase was identified on the basis of electron diffraction. As can be seen, diffusive rings are not present in this pattern and so the region may be considered fully crystalline.

Ion bombardment induces atomic rearrangements and disordering through ballistic mixing, as well as the formation of defects resulting from atomic displacements, which collectively drive the crystalline-to-amorphous transition. This is a complex phenomenon significantly influenced by irradiation parameters, the kind of implanted ion, temperature, and the intrinsic properties of the target material.[44,45]

Irradiation-induced amorphization occurs after reaching a critical irradiation dose. In both studied cases—irradiation levels of 1.2 and 6 d.p.a.—TEM analysis revealed complete amorphization. It is highly likely that the critical dose for amorphization is lower than 1.2 d.p.a., though this aspect was not explored in our study. Mechanisms of amorphization under ion bombardment have been extensively investigated in

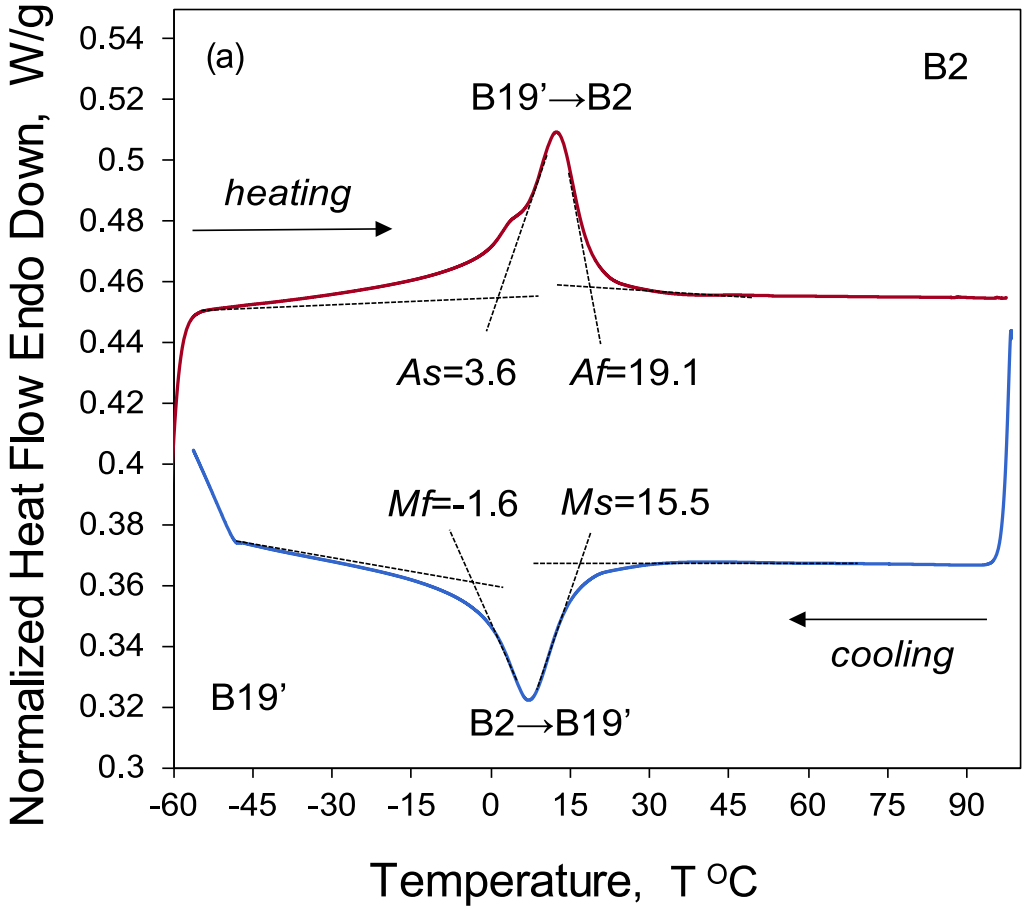

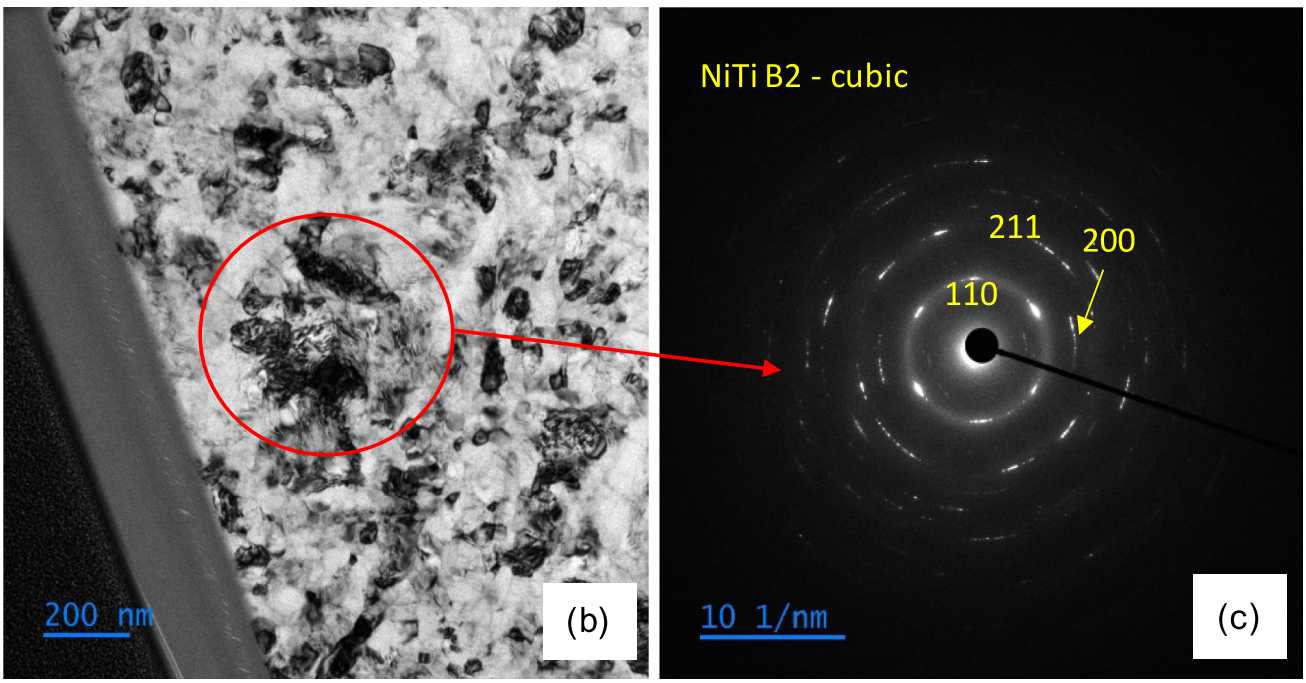

Fig. 1—DSC curve showing the characteristic temperatures of initial NiTi SMA—(*a*) and structure imaging of initial NiTi obtained by TEM—(*b*), (*c*).

recent years. Many studies suggest that amorphization arises from a combination of lattice disorder and, in some cases, the incorporation of foreign atoms, which act as disorder stabilizers.

Our results align with the findings indicating that amorphization occurs at relatively low d.p.a. levels: for instance, 0.3 and 0.15 d.p.a. after 5 MeV irradiation,[46] and 0.05 d.p.a. after 3 MeV Ni^{2+} irradiation of NiTi.[47,48] The dose-dependent nature of the amorphous transformation in NiTi during irradiation is consistent with the cascade overlap model, as observed for heavy-ion irradiation (2.5 MeV Ni^{+} and 6 MeV Ta^{+}).[49]

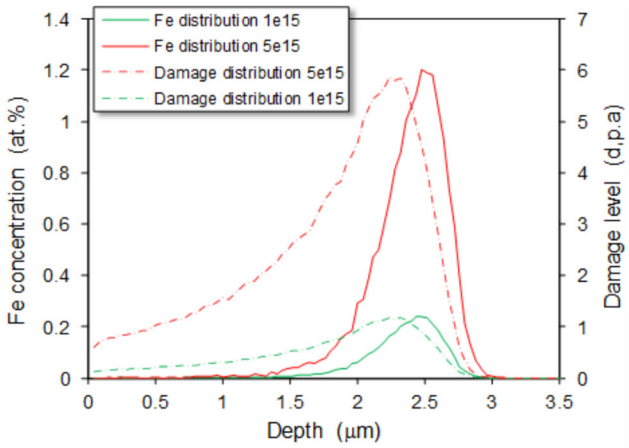

Fig. 2—Depth profiles of displacements damage (d.p.a.) and mean projected range of Fe ions calculated using SRIM code.[40]

B. *Small-Scale Mechanical Testing by Employing Two-Direction Nanoindentation Testing*

1. *P–h superelastic response in Berkovich nanoindentation test*

It is widely known that the nanoindentation method is an important technique that helps to evaluate the radiation hardening phenomenon in ion-implanted and/or irradiated materials.[50–52] Figures 5, 6, and 7 show nanoindentation results produced with the Berkovich tip. Each indentation curve and hardness value is an average of five to seven tests and error bars present the standard deviation of hardness (Figure 7).

The comparison of indentation *P–h* curves under loads of 0.2, 3.5, and 5.0 mN, obtained for non-implanted and Fe-implanted NiTi, is presented in Figure 5. It can be seen that, after high-energy Fe irradiation, NiTi shows greater stiffness; this effect is more evident for a dose of 1.2 d.p.a. compared to 6.0 d.p.a and this tendency is more evident at lower penetration depths. In the case of SMA nanoindentation, the results should be interpreted very carefully as these materials exhibit completely different stress–strain behavior from conventional elasto-plastic materials. Unlike ordinary elasto-plastic materials, SMAs may react to the indentation load through both plasticity and phase transition phenomena.

An important feature of NiTi is its superelasticity, *i.e.*, the ability to return to its initial dimensions after a relatively large deformation, when the load causing this deformation is removed. The deformations mentioned range from several to over a dozen percent, depending largely on the composition of the NiTi alloy.[1,2,4,5] In the case of the NiTi examined in this paper, the range of strain values in tensile tests (where there is an almost constant stress plateau and deformation disappears after unloading) is approximately 5 pct, as presented in our previous research, together with other NiTi SMAs.[53]

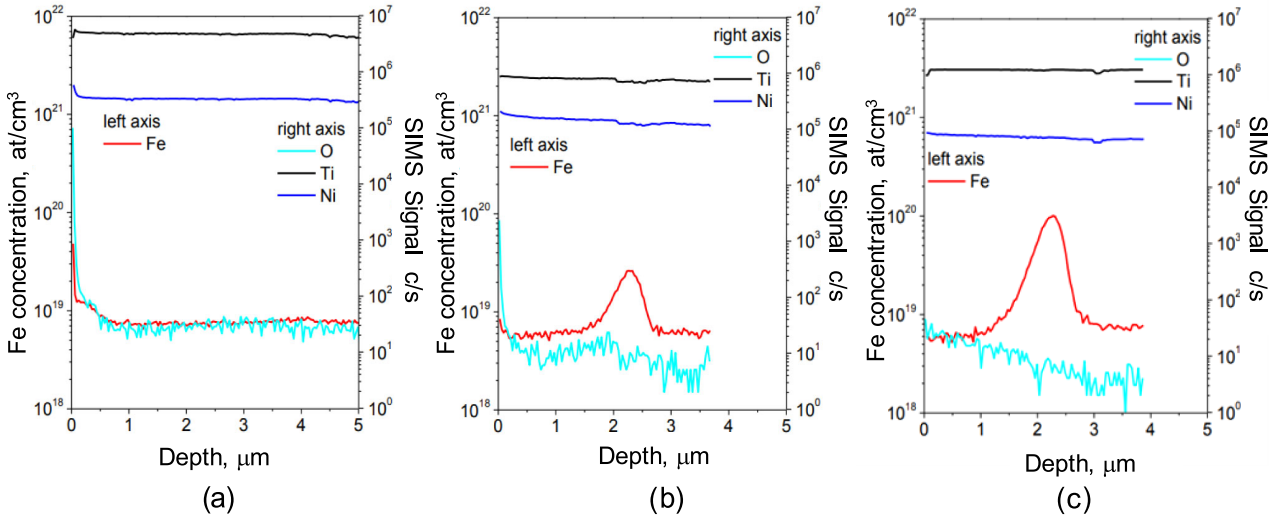

Fig. 3—Experimental SIMS depth profiles of Ni, Ti, O, and Fe distribution in NiTi: non-irradiated—(*a*), Fe^{+} ion irradiated to 1.2 d.p.a.—(*b*), Fe^{+} ion irradiated to 6 d.p.a.—(*c*).

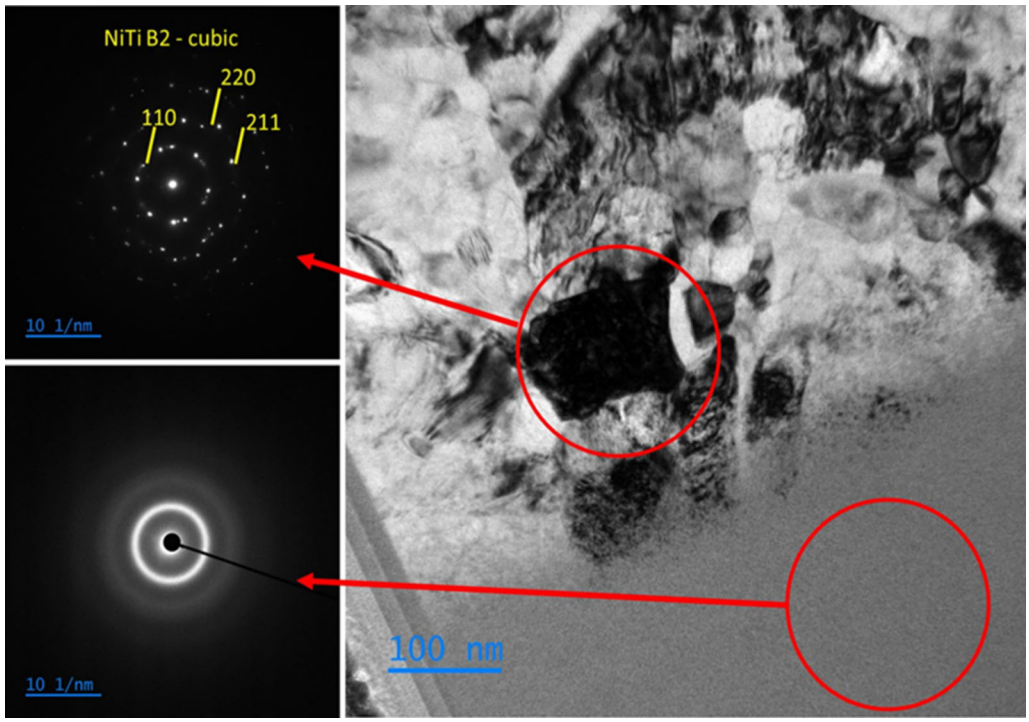

Fig. 4—Structural analysis in Bright-Field TEM image and the diffraction pattern of the irradiated to 1.2 d.p.a. NiTi: B2-crystalline structure below the ion-irradiated layer and the amorphous structure of the ion-irradiated layer (Color figure online).

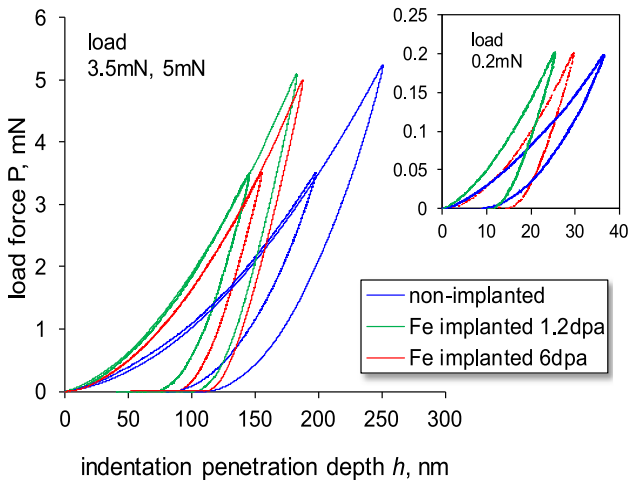

Fig. 5—Selected Berkovich load–displacement P–h curves for the NiTi before and after Fe^+ ion implantation at 1.2 and 6 d.p.a., for selected applied forces of 0.2 mN (insert), 3.5 mN, and 5 mN.

In nanoindentation tests, superelastic behavior is possible because phase transformation takes places during the loading–unloading cycle. However, above a certain applied load, the strain is not fully recoverable due to the plastic deformation of martensite generated after phase transformation. When using a sharp Berkovich tip, which creates a large strain, this situation can be observed on practically all of the load–displacement curves, see Figure 5.

One of the very promising methods for evaluating material pseudoelasticity is the calculation of the depth of recoverability through the indentation test.[54] Figure 6(a) displays a schematic indentation P–h curve for reference, where the specific values of penetration/indentation are indicated, *i.e.*, maximum depth (h_{max}) residual depth (h_{res}) and contact depth of penetration distance between the contact boundary and the summit of the indenter tip (h_c). The recoverable indentation depth (h_{recov}) is equal to the difference between h_c and residual penetration depth (h_{res}): $h_{recov} = h_c - h_{res}$. The unloading slope ($dP/dh$) is a particularly relevant parameter for estimating elastic modulus, see Figure 6(a). The grade of indent recovery (a superelastic phenomenon characteristic) is called 'the recoverability parameter' $\varphi = h_{recov}/h_{max}$, and is a measure of the pseudoelastic deformation contribution to the total deformation in the examined material.[54] The φ values for increasing load are presented in Figure 6(b). For non-irradiated samples, at the lowest load, $\varphi = 0.42$ and it diminishes when the load increases, signifying that superelasticity is most evident at the lowest load. Plastic deformation is present over the whole loading range and its contribution continuously increases with load. For Fe^+-irradiated NiTi, $\varphi = 0.18$ to 0.27 for the lowest load but decreases to 0.12 to 0.14 for a load of 1.5 N. For greater loads, there is a slight tendency for this to increase. This may be attributed to the increase in elastic modulus resulting from an increase in ion density in the implanted layer, which influences the value of φ. So, the response of the implanted sample is, qualitatively, similar to that of a non-implanted one (superelastic) but only for the lowest penetration depths, *i.e.*, in the regions of low concentrations of implanted ions. The difference between samples corresponding to different doses is very small. For the implanted samples, the φ

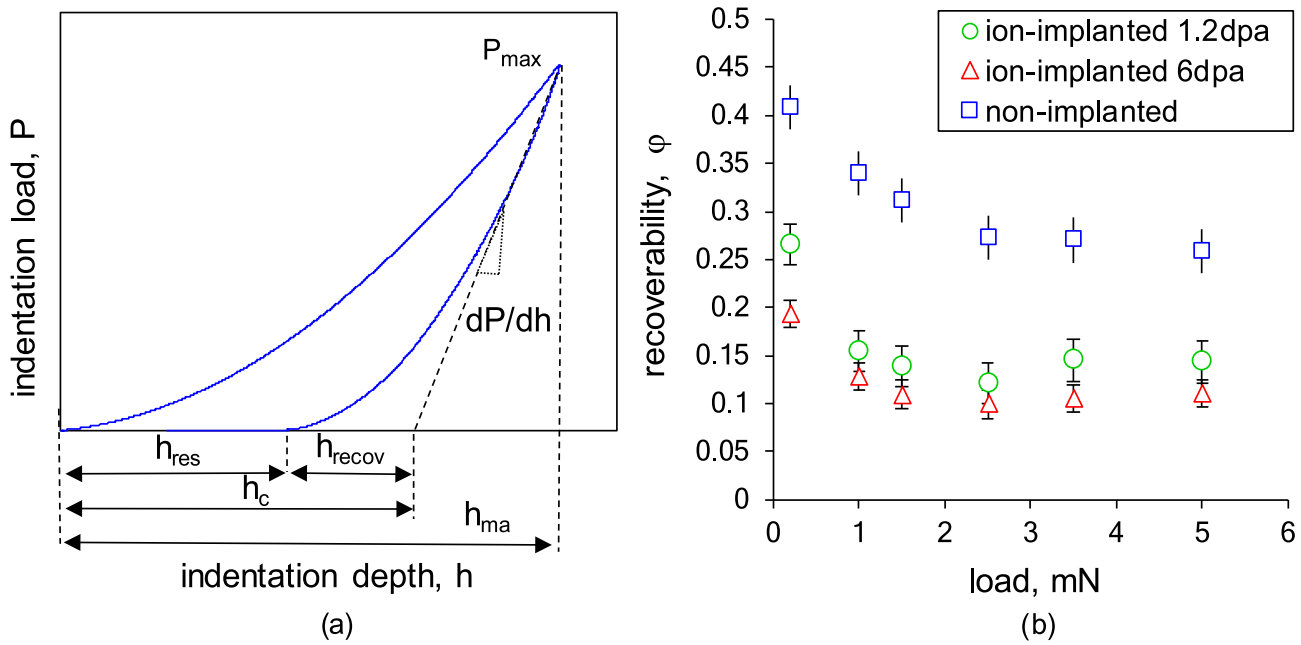

Fig. 6—Schematic of indentation *P–h* curve, for reference, with indicated specific values of penetration/indentation—(*a*); change of recoverability φ with indentation load for nanoindented by Berkovich tip non-irradiated and Fe^{+}-irradiated NiTi samples—(*b*).

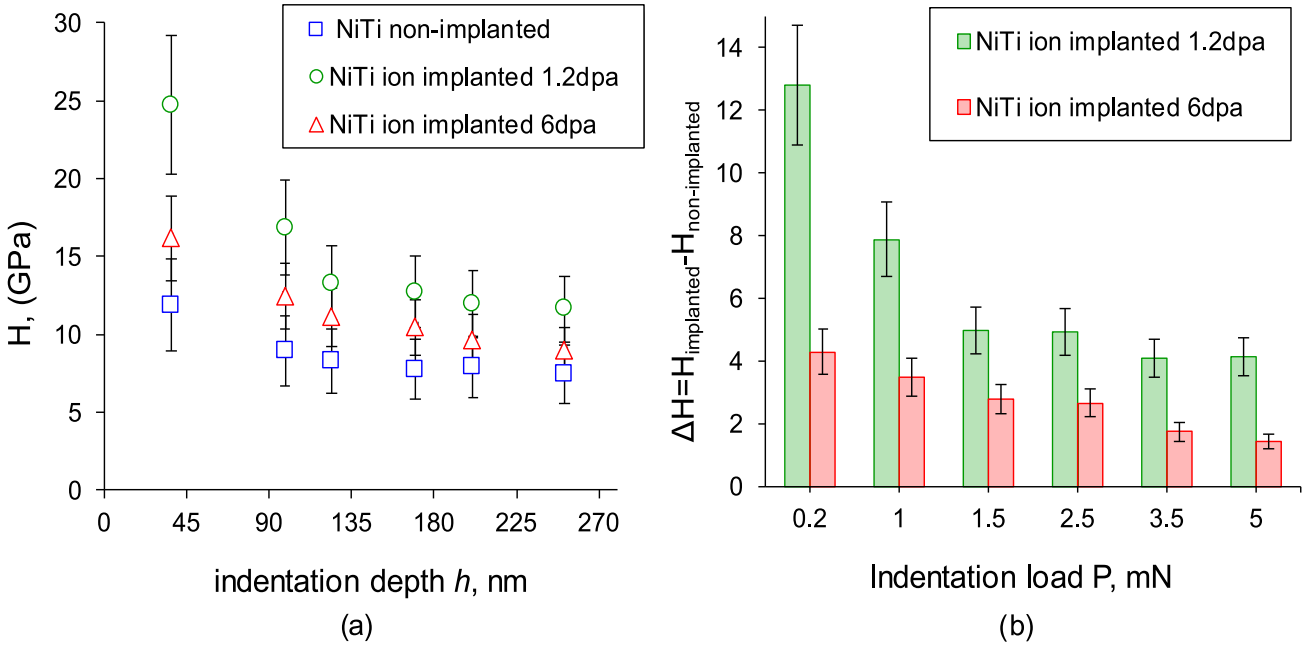

Fig. 7—Indentation-depth dependence of the averaged Berkovich hardness *H* (from 5 indents for each of the applied forces) for non-irradiated and Fe^{+} ion-irradiated NiTi samples—(*a*); ΔH change *vs.* the applied load corresponding to the indentation depth—(*b*). Indentation test along to the ion beam direction.

curve is shifted down, which means that, after implantation, the pseudoelastic effect is considerably lower for all applied loads, see Figure 6(b).

In general, this study highlights that, when assessing the functional characteristics of NiTi SMA (such as superelasticity at a sub-micron scale), the choice of adequate nanoindentation parameters is very important.

2. *Nanohardness as a function of indentation depth in conventional testing of nanoidentation along the ion beam direction*

Berkovich hardness, derived from nanoindentation testing, as a function of indentation depth along the ion beam direction for the non-implanted and ion-implanted NiTi, is shown in Figure 7(a).

First of all, it should be noted that the projected range of Fe^+ ions is located at a depth of 2.7 μm and the maximum of the damage peak is approximately 2.4 μm; the maximum indenter penetration depth is 270 nm. Hence, the indentation depth is roughly 10 times less than the thickness of the modified layer. Therefore, the depth of the indentation-affected zone approximately corresponded to the thickness of the implanted layer.[41]

Hardness changes as a function of indentation depth; Figure 7(a) shows that two stages can be observed. For low penetration depths (for both the non-implanted and ion-implanted NiTi), the hardness is influenced by the indentation size effect (ISE). When the indentation depth is smaller than 150 nm and the thickness of the indentation-affected zone is lower than 1500 nm (*i.e.*, before the Fe^+ concentration peak), the size effect manifests as a distinct increase of hardness with diminishing indentation depth (Figures 2 and 3). The increase in hardness is greater for the 1.2 d.p.a. samples, compared to the 6.0 d.p.a. samples, being more than twofold (up to 25 GPa for the 1.2 d.p.a. dose and 16 GPa for the 6.0 d.p.a. dose). It can be concluded that the material in the zone which was irradiated up to 1.2 d.p.a. is more sensitive to strain gradients than the material irradiated up to 6.0 d.p.a. (as well as the non-irradiated material). This may be attributed to the differences in material structure between the 1.2 and 6.0 d.p.a. samples (*e.g.*, different stress levels), as both samples are amorphous.

After this, the hardness decreases with increasing penetration depth, corresponding to indentation depths of 180 to 270 nm, as an average measurement of material properties in the zones having depths of 1800 to 2700 nm. In the case of unimplanted NiTi, for indentation depths of 180 to 270 nm, the value of H is approximately 6.73 GPa; whereas, the 1.2 d.p.a. irradiated sample exhibited a hardness of around 11.8 GPa. Interestingly, this value is higher than that for a 6 d.p.a. sample, which had a hardness of 9.1 GPa. Figure 7(a) shows that the hardness of both irradiated samples does not practically change with indentation depth in the indentation-affected zone (1800 to 2700 nm), where the damage peaks and ion concentrations occur (Figure 2). In other words, we cannot observe the rapid changes of hardness in the depth-area corresponding to the damage and iron concentration peaks from the conventional indentation measurements.

According to the Nix-Gao model, the relative increase in the second power of hardness is $(H^2 - H_0^2)/H_0^2 = h^*/h$. In this model, h^* is a material constant (the correction variable of the material), h is the indentation depth, and H_0 is the hardness at a macro scale. The latter would be caused by the statistically stored dislocations alone, in the absence of any geometrically necessary dislocations. Therefore, the hardness is inversely proportional to indentation depth h[55] and, for sufficiently large depths, $H \approx H_0$. In our tests, the latter equality is fulfilled for the depth range 180 to 270 nm for non-implanted samples while, for implanted samples, the increase of H with diminishing h is very small in this depth range. Therefore, for this range we can assume that the ISE does not practically affect the hardness.

High-energy ion irradiation leads to the creation of radiation defects and residual stresses in the irradiated layer; consequently, it causes changes in nanomechanical properties. This phenomenon is partially known as the 'irradiation hardening effect.'[21,22] Figure 6(a) presents NiTi nanohardness for both 1.2 and 6.0 d.p.a., corresponding with the irradiation hardening in the modified layer of 2.7 μm (according to TEM). The difference in hardness between the initial and Fe^+ ion-irradiated NiTi is plotted in Figure 7(b) based on the equation: $\Delta H = H_{implanted} - H_{non\text{-}implanted}$.

The key point in the irradiated material studies is to obtain a material response corresponding to a given level of damage. For the nuclear industry, in the context of appropriate material application, evaluating the hardness at particular radiation damage levels, over a wide range of doses, is extremely valuable. However, according to the results presented above, these data cannot be precisely specified using indentation along the ion beam, for the following reasons [some of which are illustrated in Figure 8(a)]:

Inhomogeneous damage profile Ion beam irradiation does not create a homogeneous damage distribution, see Figure 2. The fact that indentation-affected zone depth encloses micro-areas with varying degrees of damage causes that practically all indents probe regions of different doses, see Figure 8(a). This begs the question as to what is truly being tested, if not the hardness corresponding to one level of d.p.a. This makes it difficult to establish a true correlation between d.p.a. and hardness.

Inhomogeneous Fe distribution profile The implanted ions create a non-homogeneous distribution of Fe concentration, which leads to a change in the chemical composition of the modified layer, see Figures 2 and 3. Thus, in the case of indentation along the ion beam, the material with a wide Fe concentration range is probed, especially for greater penetration depths (180 to 260 nm), see Figure 8(a).

The indentation size effect (ISE) The determination of thin layer properties requires the testing to be carried out at low penetration depths, as the zone affected by the indentation should not exceed the thickness of the layer. The ISE occurs at low penetration depths, due to geometrically necessary dislocations as the indenter penetrates the material. Ion implantation leads to defects in near-surface areas and changes the type and concentration of dislocations, *i.e.*, it modifies the ISE. In other words, in ion-irradiated material, the irradiation-induced defects will add additional hardening that cannot be explained using only the geometrically necessary dislocations. This additional hardening varies at different depths because the distribution of the defects is non-uniform (*i.e.*, the layer is not homogeneous). The maximum damage levels occur at a certain distance from the surface and deeper indentations are more affected by defects. Therefore, based on the difference in hardness between the irradiated and non-irradiated samples, we can only make a rough estimate of the effect of the Fe^+ ion irradiation.

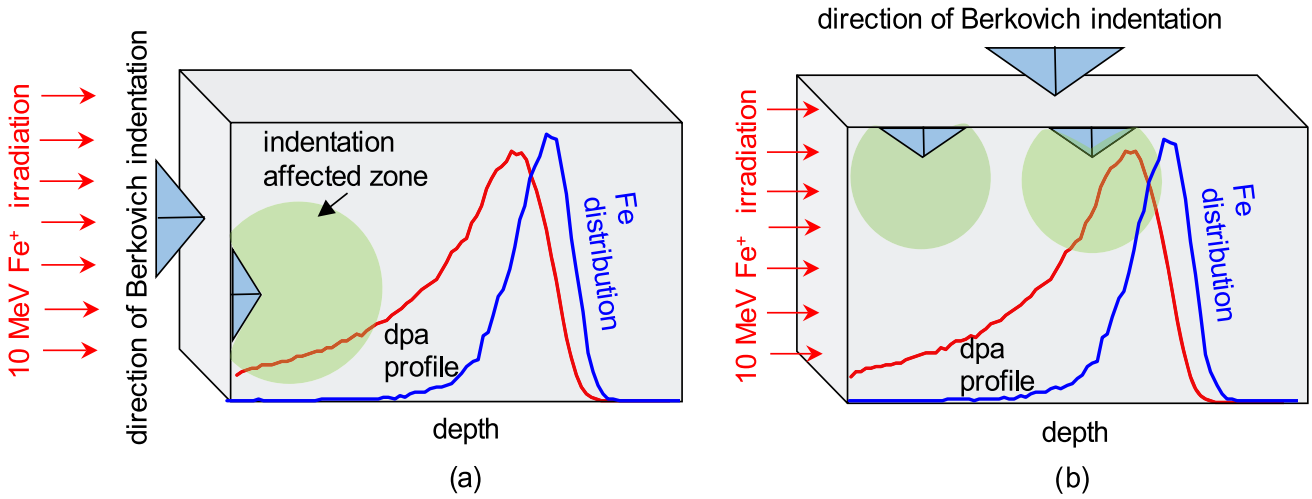

Fig. 8—Illustrative view of two approaches of hardness measurements, with marked damage profile calculated from SRIM for 10 MeV Fe^+-irradiated NiTi and indentation-affected zone: indentation test along to the ion beam direction—(*a*), indentation test perpendicular to the ion beam direction, cross-sectional nanoindentation—(*b*).

3. *Nanohardness as a function of distance from the surface in cross-sectional nanoindentation, performed perpendicular to the ion beam direction*

As explained above, when the Fe^+ ions and d.p.a. distributions are highly inhomogeneous, then the hardness determined from indentation along the direction of the ion beam corresponds to the averaged properties and cannot be attributed to the actual values of the iron concentration and d.p.a. level. Therefore, in our investigation, the NiTi hardening caused by Fe^+ ion irradiation was also measured on the cross section of samples as a function of the distance from the irradiated surface into the bulk, by using a single, low load of 0.2 mN. Such a methodology has been studied before and recent works successfully demonstrated the possibility of cross-sectional nanoindentation of ion-irradiated materials.[56–58] Figure 8 illustrates a scheme of the nanoindentation test conducted in our study, using two approaches: indentation along the ion beam direction (a) and indentation perpendicular to the ion beam direction (b).

The reliable measurement of cross-sectional hardness is certainly a challenging task, requiring special sample preparation as well as a non-standard approach. We used a cross-sectional indentation, in such a way that the probing step between the indents Δx, which is the distance projected onto the axis $0X$ (from the surface to the bulk), was sufficiently small, see Figure 9. The angle β, between the direction of the indented row and the irradiated surface, was 12 deg. The advantage of such indenting is that it provides a larger area for indentation by 'stretching out' the ion-irradiated layer, enabling a better resolution of measurement and providing direct access to the particular zones of the damaged layer (Figure 9). The probing step obtained was $\Delta x = 0.27$ μm. Various methods were attempted, in order to set 'point zero' from the interface of the NiTi sample and the Pt layer. It was decided that the most reliable method was to perform indentation from the Pt layer

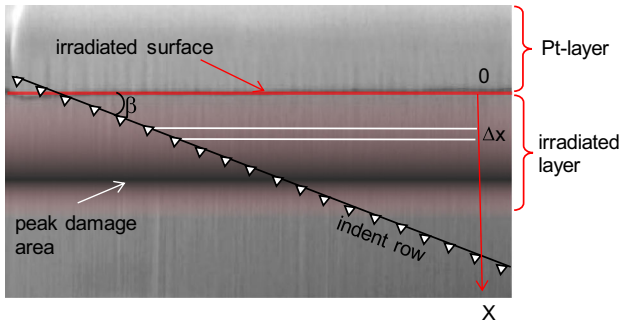

Fig. 9—Proposed arrangement of an indentation test during hardness measurement on a cross section of non-irradiated and Fe^+ ion-irradiated NiTi samples.

and record a sharp jump of hardness value at the 'zero point.'

To avoid interaction between indents located so close together, we selected a load of 0.2 mN for the indentation test on the cross section. Although the imprints for such a low load are affected by ISE, this effect is similar across all of the tested points on the cross section affected by different amounts of implanted ions (Figures 2 and 3). This approach enables variation in hardness, with respect to the distance from the surface, to be shown for a nearly constant penetration depth and, consequently, for a similar size effect.

Figure 10 shows the distribution of hardness as a function of the distance X from the surface, obtained by cross-sectional nanoindentation of non-irradiated and Fe ion-irradiated NiTi. Three parallel rows were made and the data in Figure 10 represent the average of three corresponding measurement points in the indent rows (Figure 9); each indent row had a length of 18 μm. The hardness profiles for both irradiated samples were closely related to the Fe^+ distribution profile, see Figure 2. When the distance from the surface increases (hence the concentration of Fe atoms), the hardness

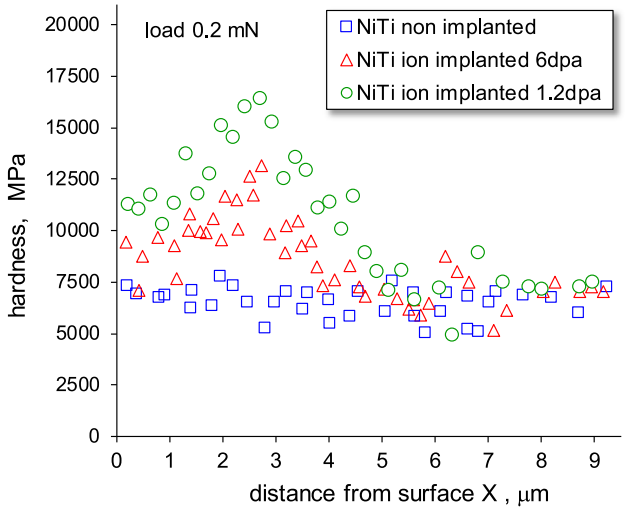

Fig. 10—Nanohardness distribution with respect to distance from surface (irradiation depth) of non-irradiated and high-energy Fe^+ ion irradiated to 1.2 and 6 d.p.a. NiTi, obtained by cross-sectional nanoidentation with a Berkovich indenter tip under the load of 0.2mN.

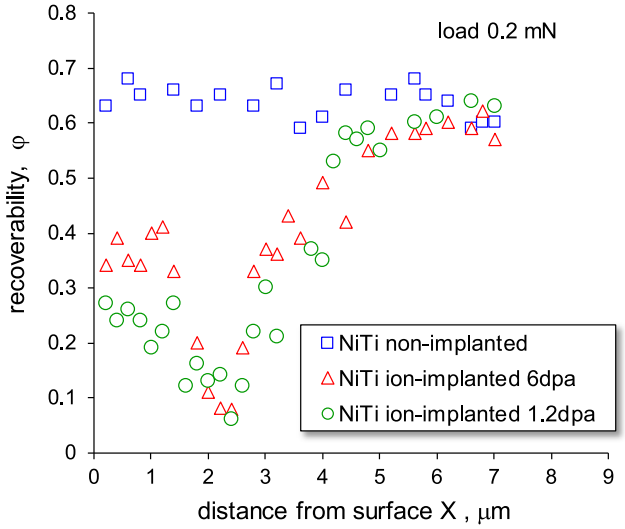

Fig. 11—Variation of recoverability parameter φ in relation to distance from surface for non-irradiated and high-energy Fe^+ ion irradiated to 1.2 and 6 d.p.a. NiTi, obtained by cross-sectional nanoidentation with a Berkovich indenter tip under the load of 0.2mN.

increases, with the highest value occurring at the maximum Fe^+ concentration, see Figure 10. The highest hardness value for the 1.2 d.p.a. sample (16.4 ± 0.42 GPa) was achieved 2.71 μm from the surface. Similarly, for the 6.0 d.p.a. sample, the maximum hardness 13.4 ± 0.39 GPa was reached at 2.74 μm. It can be observed that, starting from 2.74 μm, the hardness of the irradiated samples gradually decreases with distance X and, at 4.2 μm, it achieves the value corresponding to the non-implanted NiTi, *i.e.*, approximately 7.3 ± 0.88 GPa (see Figure 10).

The higher hardness of the 1.2 d.p.a. sample indicates that hardness decreases when the concentration of implanted ions exceeds a certain level. However, the presence of Fe ions increases the hardness of samples irradiated with both doses, compared with the non-irradiated sample. So, irradiation hardening takes place. Other authors (*e.g.*,[59,60]) have observed a non-monotonic increase in hardness with an increasing dose in the materials irradiated with Fe ions (*e.g.*, stainless steel). This phenomenon has been partially explained by irradiation-promoted precipitates. The issue is more complex for NiTi, which is a one-phase material where hardness depends on both plasticity and phase transformation. As is known from the literature, adding iron to the NiTi alloy at concentrations of 1.5 and 3 at. pct can lead to changes in the crystal structure and phase-transformation temperatures.[61,62] This alters the deformation characteristics, shape memory effect, and pseudoelasticity behavior, all of which influence hardness. Thus, a separate study is required to explain the non-monotonic increase of hardness with Fe ion concentration in NiTi.

Using the cross-section indentation method, a specific hardness value can be associated with a specific dose, if it can be assured that only irradiated material is sampled (measured) without the effect of the underlying bulk material. Some important observations can be made from Figure 10. It is clear that there is a simple relationship between the hardness peaks and Fe^+ distribution peaks (Figures 2 and 3). In the cross-section method, there is also a well-defined 'shoulder' region (up to ~ 1.3 μm) in the lower Fe^+ content areas, followed by a peak, while the traditional (along ion beam) method has no such distinct regions. The hardness changes detected in cross section can solely be attributed to Fe^+ ion beam irradiation because the size effect is similar for all indents, due to similar and very small penetration depths.

4. *Superelastic behavior of Fe ion-irradiated NiTi as a function of distance from the surface in cross-sectional nanoindentation, performed perpendicular to the ion beam direction*

When both d.p.a. and Fe^+ ion distributions are inhomogeneous, then the recoverability parameter φ, determined from indentation testing along the ion beam direction, corresponds to the averaged superelastic (or no) properties of the modified layer.

In the present study, the change in superelastic response of NiTi caused by Fe ion irradiation was also measured on the cross section of NiTi as a function of distance X from the surface, by using a constant load of 0.2 mN. In the nanoindentation tests performed perpendicular to the ion beam direction, a specific recoverability φ can be associated with a specific d.p.a. level. The recoverability values φ are presented as a function of distance X from the surface in Figure 11.

In the case of non-implanted NiTi, the φ value is almost constant, *i.e.*, 0.65 to 0.68 over the whole of the tested cross-sectional area. For ion-implanted samples, up to a distance from the surface of 1.4 μm, the value of φ is 0.23 to 0.27 and 0.35 to 0.38 for 1.2 and 6.0 d.p.a., respectively. At larger distances (X), the recoverability parameter φ diminishes.

The recoverability parameter φ reaches the minimum value of 0.07 at a distance of ~ 2.5 μm and then increases to a value of 0.65, maintaining this value until a distance exceeding 4.8 μm from the surface. This indicates that superelasticity is mostly reduced at distances around 2.5 μm from the surface. The difference in φ values between both levels of d.p.a. is noticeable. For samples irradiated up to 1.2 d.p.a., the φ values are lower, meaning that the pseudoelastic effect is reduced after implantation, see Figure 11.

Cross-sectional nanoindentation tests of irradiated NiTi samples indicate that the hardness profile reflects the Fe ion concentration profile and the recoverability φ profile reflects the d.p.a. profile (Figures 10 and 11). Figures 10 and 11 show that, at a distance of approximately 5 μm from the surface, the values of φ and the hardness of initial and ion-irradiated NiTi are similar. This is significantly beyond the irradiated depth range, *i.e.*, significantly deeper than the thickness of the ion-irradiated layer. This may be associated with the complex residual stress condition after ion implantation. Once again, this confirms the rationality and relevance of the cross-sectional nanoindentation tests performed perpendicular to the ion beam direction.

Further work, particularly on the correlation of the structure and mechanical behavior of high-energy ion-irradiated NiTi, is necessary to elucidate the subtle SMA micromechanical properties in the indentation test.

IV. CONCLUSIONS

In this paper, we studied Fe^+ ion-irradiated NiTi SMA at a high energy of 10 MeV and at damage levels of 1.2 and 6.0 d.p.a. The ion penetration depth was around 3 μm, as estimated by the SRIM code and confirmed by SIMS analysis. The amorphization of the irradiated layer was observed by TEM and the mechanical response, such as nanohardness and elastic recoverability φ, was determined by nanoindentation tests.

Two-direction nanoindentation tests were used. The first direction involved the indentation of the irradiated surface along the ion beam direction, while the second applied to the indents on a cross-sectional surface perpendicular to the ion beam direction.

These two types of tests are referred to as classical hardness and cross-sectional hardness, respectively. If the first type of test is used, there are some limitations: the hardness and elastic recovery corresponding to a given damage level or a given Fe ion concentration cannot be precisely specified because these quantities vary greatly with indenter penetration depth (and with the distance from the irradiated surface).

Therefore, to study the hardness and local phase transformation in near-surface regions, a second, complementary, approach was proposed, in which the indents were made on the cross-section surface.

The cross-sectional indentation has the benefit of allowing the determination of the local hardness corresponding to a small region irradiated with a specific dose of ions, which can be assumed to be locally constant. Consequently, when applied at different distances from the NiTi sample surface, it better reveals the variation of mechanical properties that occurs along the beam penetration depth.

The hardness distribution on the cross section indicates the formation of an irradiation-hardened layer and the maximum hardness (2.5 times greater than non-irradiated NiTi) occurs at a distance of ~ 2.71 μm from the irradiated surface. The examination of the hardness of Fe-irradiated NiTi also shows that the differences in mechanical properties between two irradiation fluencies can be attributed to the different concentration of iron atoms implanted during high-energy implantation.

The distribution of recovery parameter φ shows that the high-energy Fe^+ ion irradiation suppresses NiTi superelasticity, this effect being the greatest at a distance of 2.4 μm from the irradiated surface. The observed changes in superelastic properties were achieved by the amorphous layer, which tames the B2-B19′ phase transformation at a sub-micron scale.

It has also been shown that the maximum hardness value corresponds to the maximum Fe^+ concentration; in both samples, the maximum hardness was measured at the same depth (2.7 μm). The position of the damage peak and maximum value of recoverability φ from the surface is located closer to the surface at 2.4 μm. Furthermore, it is worth noting that the changes in the hardness and φ parameters were measured far behind the Fe^+ ion range; this may be attributed to the complex residual stress state appearing after irradiation.

In summary, our study points out that, for estimating the functional characteristics of SMA (such as superelasticity at a sub-micron scale), the choice of an adequate nanoindentation mode and parameters is very important. We have also shown that the nanomechanical characterization of high-energy Fe^+ ion-irradiated NiTi SMA is essential for studying changes in mechanical and phase-transformation properties in near-surface regions, paving the way for SMA applications in nuclear technologies.

ACKNOWLEDGMENTS

Parts of this research were carried out at IBC at the Helmholtz-Zentrum Dresden-Rossendorf e. V., a member of the Helmholtz Association, through the implementation of RADIATE proposal no. 22003083-ST-1.1-RADIATE. We would like to thank Dr. M. May and Dr. R. Jakiela for sample preparation and SIMS measurement.

AUTHOR CONTRIBUTIONS

Neonila Levintant-Zayonts: methodology, investigation, writing—review & editing, supervision, and conceptualization; Iwona Jozwik: data curation and writing—review & editing; Witold Chrominski:

investigation and data curation; Shavkat Akhmadaliev: data curation; Stanislaw Kucharski: methodology and writing—review & editing.

CONFLICT OF INTEREST

On behalf of all authors, the corresponding author states that there is no conflict of interest.

OPEN ACCESS

REFERENCES

1. K. Otsuka and C.M. Wayman: *Shape Memory Materials*, Cambridge University Press, Cambridge, 1998, p. 2017.
2. M. Wu and L.M. Schetky: *Industrial Applications for Shape Memory Alloys, International Conference on Shape Memory and Superelastic Technologies*, Pacific Grove, CA. 2000. p. 171.
3. S. Ahmad, A.W. Hashmi, J. Singh, K. Arora, Y. Tian, F. Iqbal, M. Al-Dossari, and M.I. Khan: *J. Mater. Res. Technol.*, 2024, vol. 32, pp. 4136–97. https://doi.org/10.1016/j.jmrt.2024.08.213.
4. J.V. Humbeeck: *Mater. Sci. Eng. A*, 1999, vol. 273–75, pp. 134–48. https://doi.org/10.1016/S0921-5093(99)00293-2.
5. S. Viscuso, S. Gualandris, G. de Ceglia, and V. Visentin: *Shape Memory Alloy Engineering (Second Edition) for Aerospace, Structural, and Biomedical Applications*. 2021. pp. 609–23. https://doi.org/10.1016/B978-0-12-819264-1.00018-2.
6. T. Yoneyama and S. Miyazahi: *Shape Memory Alloys for Biomedical Applications*, Woodhead, Cambridge, 2008.
7. N.B. Morgan: *Mater. Sci. Eng. A*, 2004, vol. 378, pp. 16–23. https://doi.org/10.1016/j.msea.2003.10.326.
8. R.R. Ionaitis, V.V. Kotov, and I.M. Shchukin: *At. Energy*, 1995, vol. 79, pp. 712–14. https://doi.org/10.1007/BF02415395.
9. R.R. Ionaitis: *At. Energy*, 1997, vol. 82, pp. 388–93. https://doi.org/10.1007/BF02418737.
10. I. Ozkul, M. Ali Kurgun, E. Kalay, C. Aksu Canbay, and K. Aldas: *Eur. Phys. J. Plus*, 2019, vol. 585, pp. 2–15. https://doi.org/10.1140/epjp/i2019-12925-2.
11. V.I. Bobrovskii, S.V. Afanasyev, V.I. Voronin, V.A. Kazantsev, N.V. Kataeva, V.D. Parkhomenko, N.V. Proskurnina, and V.V. Sagaradze: *Phys. Met. Metallogr.*, 2024, vol. 125, pp. 211–16. https://doi.org/10.1134/S0031918X23602664.
12. P. Sharma, P.N. Maya, A. Satyprasad, and S.P. Deshpande: *Metall. Mater. Trans. A*, 2024, vol. 55A, pp. 2932–39. https://doi.org/10.1007/s11661-024-07449-x.
13. G.S. Was, J.T. Busby, T. Allen, E.A. Kenik, A. Jensson, S.M. Bruemmer, J. Gan, A.D. Edwards, P.M. Scott, and P.L. Anderson: *J. Nucl. Mater.*, 2002, vol. 300, pp. 198–216. https://doi.org/10.1016/S0022-3115(01)00751-6.
14. K. Nordlund, S.J. Zinkle, A.E. Sand, F. Granberg, R.S. Averback, R.E. Stoller, T. Suzudo, L. Malerba, F. Banhart, W.J. Weber, F. Willaime, S.L. Dudarev, and D. Simeone: *J. Nucl. Mater.*, 2018, vol. 512, pp. 450–79. https://doi.org/10.1016/j.jnucmat.2018.10.027.
15. P. Changizian, Z. Yao, C. Lu, F. Long, and M.R. Daymond: *J. Nucl. Mater.*, 2019, vol. 15, pp. 1–13. https://doi.org/10.1016/j.jnucmat.2018.11.040.
16. C.H.M. Broeders and A.Y. Konobeyev: *J. Nucl. Mater.*, 2004, vol. 328, pp. 197–214. https://doi.org/10.1016/j.jnucmat.2004.05.002.
17. C.R.F. Azevedo: *Eng. Failure Anal.*, 2011, vol. 18, pp. 1921–42. https://doi.org/10.1016/j.engfailanal.2011.06.008.
18. J. Lee, C.R. Lear, X. Zhang, P. Bellon, and R.S. Averback: *Metall. Mater. Trans. A*, 2015, vol. 46, pp. 1046–061. https://doi.org/10.1007/s11661-014-2704-4.
19. Z. Świątek, N. Levintant-Zayonts, M. Michalec, T. Czeppe, M. Lipinski, O. Bonchyk, and H. Savytskyj: *Phys. Proc.*, 2010, vol. 10, pp. 69–76. https://doi.org/10.1016/j.phpro.2010.11.077.
20. P. Hosemann: *Scripta Mater.*, 2018, vol. 143, pp. 161–68. https://doi.org/10.1016/j.scriptamat.2017.04.026.
21. K. Vogel, C. Heintze, P. Chekhonin, S. Akhmadaliev, E. Altstadt, and F. Bergner: *Nucl. Mater. Energy*, 2020, vol. 24, p. 100759. https://doi.org/10.1016/j.nme.2020.100759.
22. A. Das, E. Altstadt, C. Kaden, G. Kapoor, S. Akhmadaliev, and F. Bergner: *Front. Mater.*, 2022, vol. 8, p. 811851. https://doi.org/10.3389/fmats.2021.811851.
23. L. Mei, X. Guo, and K. Jin: *Front. Mater.*, 2022, vol. 9, p. 849209. https://doi.org/10.3389/fmats.2022.849209.
24. D. Kiener, A.M. Minor, O. Anderoglu, Y. Wang, S.A. Maloy, and P. Hosemann: *J. Mater. Res.*, 2012, vol. 27, pp. 2724–36. https://doi.org/10.1557/jmr.2012.303.
25. K. Jin, Y. Xia, M. Crespillo, H. Xue, Y. Zhang, Y.F. Gao, and H. Bei: *Scripta Mater.*, 2018, vol. 157, pp. 49–53. https://doi.org/10.1016/j.scriptamat.2018.07.035.
26. J. Li, Y. Chen, and H. Wang: *Metall. Mater. Trans. A*, 2017, vol. 48A, pp. 1466–73. https://doi.org/10.1007/s11661-016-3895-7.
27. Ch.D. Hardie, S.G. Roberts, and A.J. Bushby: *J. Nucl. Mater.*, 2015, vol. 462, pp. 391–440. https://doi.org/10.1016/j.jnucmat.2014.11.066.
28. G. Pan, Z. Cao, J. Shi, M. Wei, L. Xu, and X. Meng: *Sens. Actuators A*, 2014, vol. 217, pp. 75–80. https://doi.org/10.1016/j.sna.2014.06.019.
29. X. Gao, D. Hong, H.M. Paranjape, W. Zhang, and P.M. Anderson: *Int. J. Mech. Sci.*, 2024, vol. 270, p. 109077. https://doi.org/10.1016/j.ijmecsci.2024.109077.
30. H. Wang, X. Yi, Y. Zhu, Y. Yin, Y. Gao, W. Cai, and Z. Gao: *Appl. Surf. Sci.*, 2017, vol. 419, pp. 91–97. https://doi.org/10.1016/j.apsusc.2017.05.021.
31. N. Afzal, I.M. Ghauri, F.E. Mubarik, and F. Amin: *Physica B: Condens. Matter.*, 2011, vol. 406, pp. 8–11. https://doi.org/10.1016/j.physb.2010.09.040.
32. H. Wang, X. Yi, Y. Zhu, Y. Yin, Y. Gao, W. Cai, and Z. Gao: *Appl. Surf. Sci.*, 2017, vol. 419, pp. 91–97. https://doi.org/10.1016/j.apsusc.2017.05.0210169-4332.
33. T.B. Lagrange and R. Gotthard: *Optoelectron. Adv. Mater. Rapid Commun. M*, 2003, vol. 5, pp. 313–18.
34. T. La Grange, C. Abromeit, and R. Gotthardt: *Mater. Sci. Eng. A*, 2006, vol. 438–440, pp. 521–26. https://doi.org/10.1016/j.msea.2006.02.056.
35. T. Lagrange, R. Schäublin, D.S. Grummon, C. Abromeit, and R. Gotthardt: *Philos. Mag.*, 2005, vol. 85, pp. 577–87. https://doi.org/10.1080/02678370412331320107.
36. X.T. Zu, S. Zhu, X. Xiang, L.P. You, Y. Huo, and L.M. Wang: *Mater. Sci. Eng. A*, 2003, vol. 363, pp. 352–55. https://doi.org/10.1016/S0921-5093(03)00635-X.
37. J. Cheng and A.J. Ardell: *Nucl. Instrum. Methods Phys. Res. Sect. B: Beam Interact. Mater. At.*, 1990, vol. 44, pp. 336–43. https://doi.org/10.1016/0168-583X(90)90648-E.
38. D.S. Grummon and R. Gotthardt: *Acta Mater.*, 2000, vol. 48, pp. 635–46. https://doi.org/10.1016/S1359-6454(99)00401-2.
39. A. Hinojos, D. Hong, H. Sriram, L. Feng, C. Yang, J.P. Wharry, X. Gao, K. Hattar, N. Li, J.E. Schaffer, Y. Wang, M.J. Mills, and P.M. Anderson: *Scripta Mater.*, 2023, vol. 226, p. 11526. https://doi.org/10.1016/j.scriptamat.2022.115261.
40. J.F. Ziegler, J.P. Biersack, and U. Littmark: *The Stopping and Range of Ions in Solids*, Pergamon Press, New York, 1985.
41. W.C. Oliver and G.M. Pharr: *J. Mater. Res.*, 2004, vol. 19, pp. 3–20. https://doi.org/10.1557/jmr.2004.19.1.3.

42. A.D. Pogrebnjak, S.N. Bratushka, V.M. Beresnev, and N. Levintant-Zayonts: *Russ. Chem. Rev*., 2013, vol. 82, pp. 1135–59. https://doi.org/10.1070/RC2013v082n12ABEH004344.
43. S. Kucharski, N. Levintant-Zayonts, and J. Luckner: *Mater. Des*., 2014, vol. 56, pp. 671–79. https://doi.org/10.1016/j.matdes.2013.11.056.
44. D.E. Pedraza: *Metall. Trans. A*, 1990, vol. 21A, pp. 1809–15.
45. A.T. Motta: *J. Nucl. Mater*., 1997, vol. 244, pp. 227–50.
46. T. La Grange and R. Gotthardt: *Scripta Mater*., 2004, vol. 50, pp. 231–36. https://doi.org/10.1016/j.scriptamat.2003.09.017.
47. P.J. Maziasz, N.H. Packan, D.F. Pedraza, and E.H. Lee, *TEM Study of Amorphization in NiTi Irradiated With Ni^{2+} Ions at Room Temperature*. Oak Ridge National Laboratory, Oak Ridge, TN, 1987.
48. D.F. Pedraza: *Metall. Trans. A*, 1990, vol. 21A, pp. 1809–15.
49. J.L. Brimhall, H.E. Kissinger, and A.R. Pelton: *Rad. Effect*, 1985, vol. 90, pp. 241–58. https://doi.org/10.1080/00337578508222535.
50. P. Hosemann, D. Kiener, Y. Wang, and S.A. Maloy: *J. Nucl. Mater*., 2012, vol. 425, pp. 136–39. https://doi.org/10.1016/j.jnucmat.2011.11.070.
51. P. Changizian, A. Brooks, Z. Yao, and M.R. Daymond: *Metall. Mater. Trans. A*, 2018, vol. 49A, pp. 498–514. https://doi.org/10.1007/s11661-017-4445-7.
52. N. Levintant-Zayonts, G. Starzynski, and S. Kucharski: *J. Tribol*., 2024, vol. 147, p. 011401. https://doi.org/10.1115/1.4066204.
53. N. Levintant-Zayonts, G. Starzyński, M. Kopeć, and S. Kucharski: *Tribol. Int*., 2019, vol. 137, pp. 313–23. https://doi.org/10.1016/j.triboint.2019.05.005.
54. S.S. Kumar, I.A. Kumar, L. Marandi, and I. Sen: *Acta Mater*., 2020, vol. 201, pp. 303–15. https://doi.org/10.1016/j.actamat.2020.09.080.
55. W.D. Nix and H. Gao: *J. Mech. Phys. Solids*, 1998, vol. 46, pp. 411–25. https://doi.org/10.1016/S0022-5096(97)00086-0.
56. A. Lupinacci, K. Chen, Y. Li, M. Kunz, Z. Jiao, G.S. Was, M.D. Abad, A.M. Minor, and P. Hosemann: *J. Nucl. Mater*., 2015, vol. 458, pp. 70–76. https://doi.org/10.1016/j.jnucmat.2014.11.050.
57. C.K. Dolph, D.J. da Silva, M.J. Swenson, and J.P. Wharry: *J. Nucl. Mater*., 2016, vol. 481, pp. 33–34. https://doi.org/10.1016/j.jnucmat.2016.08.033.
58. M. Saleh, A. Xu, Ch. Hurt, M. Ionescu, J. Daniels, P. Munroe, L. Edwards, and D. Bhattacharyya: *Int. J. Plast*., 2019, vol. 112, pp. 242–56. https://doi.org/10.1016/j.ijplas.2018.08.015.
59. M. Liu, J. Nie, and P. Lin: *Front. Mater*., 2022, vol. 9, pp. 1–14. https://doi.org/10.3389/fmats.2022.823539.
60. M. Sun, L. Yu, and X. Xiao: *J. Mater. Res. Technol*., 2023, vol. 22, pp. 3101–107. https://doi.org/10.1016/j.jmrt.2022.12.122.
61. B.D. Ingale, W.C. Wei, P.C. Chang, Y.K. Kuo, and S.K. Wu: *J. Appl. Phys*., 2011, vol. 110, p. 113721. https://doi.org/10.1063/1.3666029.
62. B. Keskin and B. Derin: *Appl. Phys. A*, 2024, vol. 130, p. 173. https://doi.org/10.1007/s00339-024-07306.